Design and Application of Electron-Transporting Organic Materials

Marko Strukelj,* Fotis Papadimitrakopoulos, Timothy M. Miller,* Lewis J. Rothberg

Operating lifetime is the main problem that complicates the use of polymeric light-emitting diodes (LEDs). A class of electron transport (ET) polymers [poly(aryl acrylate) and poly(aryl ether)s] is reported in which moieties with high electron affinities are covalently attached to stable polymer backbones. Devices based on poly(*p*-phenylenevinylene) (PPV) prepared with these materials exhibited a 30-fold improvement in stability and, in one case, dramatically lower (10 volts versus about 30 volts) operating voltage relative to those having conventional ET layers. The current-carrying capacity of indium tin oxide–PPV–polymeric ET layer–aluminum LEDs was also increased by a factor of 30. These improvements lead to an enhancement in power efficiency of nearly an order of magnitude. Choosing polymers with high glass transition temperatures increases device lifetime.

Polymeric LEDs have gained considerable attention since 1990, when a group at Cambridge University (*1*) reported that PPV devices exhibit electroluminescence (*2–10*). Interest in organic LEDs is fueled by the large market for indicators and flat panel displays. In principle, such displays might be simpler to design and manufacture than active matrix liquid-crystal displays and are intrinsically emissive, which is attractive to users. LEDs in which polymeric active layers are used might have several advantages over those that use evaporated films, which have been under development for some time (*11*). These advantages include high thermal stability, simplicity of manufacture, and the ability to prepare large areas. Organic LEDs require the injection of holes and electrons into the emitter layer and depend on their recombination to yield singlet excitons whose radiative decay produces visible light. A sandwich geometry is generally used in which indium tin oxide (ITO) serves as a transparent anode and a metal with a low work function (ϕ) such as Ca, Mg-Ag alloy, or Al serves as the cathode (Fig. 1). Efficient devices (with efficiency measured in terms of the number of photons per electron) require balanced injection of holes and electrons, because unipolar charge injection (that is, only electrons or only holes) cannot lead to exciton formation (*7*).

For conjugated polymers such as PPV and its derivatives, electron injection has been said to limit device efficiency when the anode is ITO (*2, 4, 8*). Lowering the work function of the cathode by changing from Al (ϕ = 4.3 eV) to Ca (ϕ = 2.9 eV) has improved the quantum efficiency of PPV devices (photon emitted per injected electron) from 0.002 to 0.1% (*7*). Unfortunately, Ca reacts extremely rapidly with moisture and is therefore unattractive for this purpose. Incorporation of an ET material between the cathode and PPV (*4*) further improves quantum efficiency by confining holes to the emissive PPV layer and preventing unipolar current flow. The ET layer also improves power efficiency by facilitating electron injection from the cathode, thereby permitting the use of more stable metals such as Al without dramatically reducing the quantum efficiency. The ET layer also diminishes exciton quenching near the metal electrode by acting as a spacer.

One widely used ET material is 2-(4-biphenylyl)-5-(4-*tert*-butylphenyl)-1,3,4-oxadiazole (PBD) (Fig. 2) (*12*). This compound crystallizes readily in thin film form (500 Å), and, as a result, it is generally dissolved in an inert amorphous polymer matrix [for instance, poly(methyl methacrylate) (PMMA)] (*4*). However, there are drawbacks to this approach. Dilution of the active species by the polymer diminishes the conductivity (*13*) and increases the operating voltage of the device. The achievable loading is limited by solubility (for PBD-PMMA it is 3:1 by weight or 46 mol % of PBD), and eventual macroscopic phase separation after film preparation often results in device failure. Recently, it has been reported that 3-(4-biphenylyl)-4-phenyl-5-(4-*tert*-butylphenyl)-1,2,4-triazole (TAZ) (Fig. 2) also transports electrons and, in addition, appears to block holes better than PBD (*14*); the morphology of TAZ films was not discussed. Organic materials tend to be *p*-type (that is, preferentially transport holes), presumably because of their low electron affinities, and the majority of emitters therefore require *n*-type ET companion layers which, for the same reason, are difficult to design.

In this report, we describe the synthesis and use of a series of electron-deficient oxadiazole-, triazole-, quinoxaline-, and triazine-containing materials as ET layers in PPV-based LEDs. Two were used directly as thin monomeric films containing 100% electroactive species, whereas the others were covalently incorporated in high concentration in high molecular weight polymers. The materials were designed to be amorphous so as to minimize potential problems due to crystallization. They were also designed to have a variety of electroactive components as well as ranges of glass-transition temperatures (T_g's), lowest unoccupied molecular orbital (LUMO or conduction level) energy levels, and a variety of concentrations of electroactive groups. Finally, we required the polymers to have good solubility in common solvents. The resulting range of observed performance enables us to reach several important conclusions about the relative importance of band offsets (difference between the LUMO energy level and the cathode ϕ) and transport properties on the performance and stability of ET materials. In particular, we show that with these materials stability can be vastly improved relative to PBD, and operating voltage (hence power consumption) can be reduced by a factor of at least 4.

The substituted 2,3-diphenylquinoxaline **1** (Fig. 2) was prepared from the corresponding benzil (*15*) by reaction with *o*-phenylenediamine, and the triazine **2** is commercially available. Poly(methacrylate) **3** was prepared by conventional free-radical polymerization of the monomer (Fig. 3). We prepared the poly(aryl ether)s **4** to **6** from the appropriate biphenol (**7** or **8**) and activated aromatic difluoride (**9** or **10**), yielding high molecular weight linear polymers (*16*) by using a dipolar aprotic solvent and anhydrous potassium carbonate (K_2CO_3) as the base (Fig. 3). The 3,5-di-*tert*-butyl–substituted phenolate pendant groups of **1** and the *meta* substitution of the substituted triazine moieties at the pyridine group of **2** were chosen to introduce disorder and deter crystallization of the evaporated films. Similarly, the *meta* substitution of the O linking group in the poly(aryl ether)s ensures high solubil-

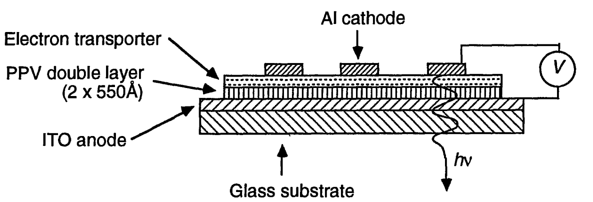

Fig. 1. Structure of the LED devices.

AT&T Bell Laboratories, Murray Hill, NJ 07974, USA.

*To whom correspondence should be addressed.

ity and suppresses crystallization. These ET materials appear to be amorphous, as determined by differential scanning calorimetry; no crystallization exotherm was detectable. The T_g's for compounds **1** and **2** are 77° and 109°C, respectively, whereas those of polymers **3** to **6** ranged from 153° to 186°C (Table 1). Adherent, smooth, thin films of these materials could be easily deposited on various substrates. A solution (0.060 g of PBD and 0.020 g of PMMA) was prepared in the melt to compare the T_g's of the new materials to that of PBD-PMMA. On cooling, a transparent and essentially colorless glassy solid was obtained. However, heating (10°C/min) from 30° to 120°C resulted in the formation at 59°C of an opaque solid due to PBD crystallization, indicating that this composite is unstable to mild heating that might be encountered during device fabrication or operation.

All of the devices tested were composed of two thin layers of organic material sandwiched between ITO and Al electrodes (Fig. 1). One layer was the emitter PPV (~1100 Å), and the other was the electron transporter (500 to 600 Å). Compounds **1** and **2** and polymers **3** to **6** were used as ET layers. The former were deposited by vacuum evaporation (~10^{-6} torr), whereas the latter were spin-coated. In addition, devices were prepared exactly as previously described with PBD-PMMA in order to permit comparison with reported LED performance (*4*). In these devices, the PBD-PMMA layer was thinner (~250 Å). The PPV was prepared by thermal conversion of the sulfonium precursor polymer at 200°C under an atmosphere of 15% H_2 in N_2 (*17*) and was deposited as two successive 550 Å layers (Fig. 1). We found that this procedure substantially reduces pinholes in PPV and yields reproducible device behavior.

The LEDs were 1 mm^2 in area and were driven with direct currents up to 5 A/cm^2, which required biases of ~10 to 60 V. Internal quantum efficiencies (photons per electron) were evaluated with a calibrated Si photodiode (*18*). We found that the quantum efficiencies of our LEDs were essentially independent of the ET layer when driven in the current range 0 to 25 mA/cm^2 and were similar to those reported (up to 0.002%) (*7*). If each of the ET materials prevents unipolar current flow and all of the electrons recombine with holes in the PPV layer, the quantum efficiency should be determined by the probability of making emissive excitons and their radiative efficiency in PPV (*19*).

The critical parameter in the practical design of devices is, however, the power efficiency, and this varies widely with choice of ET. Because the quantum efficiency is roughly constant, it is desirable to achieve the largest possible current at the minimum voltage. In this respect, the low turn-on voltage (6 to 10 V) of devices with polymer **5** represents a dramatic improvement over the turn-on voltages of the other devices, which were in the range from 18 to 32 V (Fig. 4). These LEDs are consequently about four times as power-efficient. The low operating voltage is in the range for PPV (~6 V) devices without an ET layer (*4*) while at the same time retaining the high quantum efficiency obtainable with ET layers where unipolar current is blocked.

Greenham *et al.* (*6*) recently reported that the energy level of the LUMO (conduction level) of the electron transporter and emitter poly(cyanoterephthalylidene)s is 0.9 eV lower than the energy level of the LUMO of PPV. This energy level provides a closer match to the work function of Al to give quantum efficiencies that were reported to be the same for devices with Al or Ca cathodes (*6*). We used cyclic voltammetric reduction potential values as a surrogate for LUMO energy levels. Reductions of polymers **3** to **6** in solution were irreversible, presumably because of polymer precipitation, in polyanionic form, onto the electrode upon reduction, and as a result model compounds **11** to **15** (Fig. 2) were prepared and evaluated instead (*20*). The reduction potentials of **11** to **15**, and of **1** and **2**, are compiled in Table 1. Although reduction potentials range from −1.27 V for 4,4′-dimethoxybenzil (**14**) to −2.16 V for **12**, there appears to be no correlation between these values and either the efficiency or the turn-on voltages of the corresponding devices. One might expect that, because the reduction potentials of **1**, **2**, and **6** were significantly higher than those of PBD and **3** through **5**, electron injection from the cathode should be improved. Apparently electron injection is not improved by reducing the band offsets, and we conclude that the determining factor in increasing currents must therefore be the space charge limit imposed by the mobility of the ET

Fig. 2. Monomeric ET compounds and model compounds.

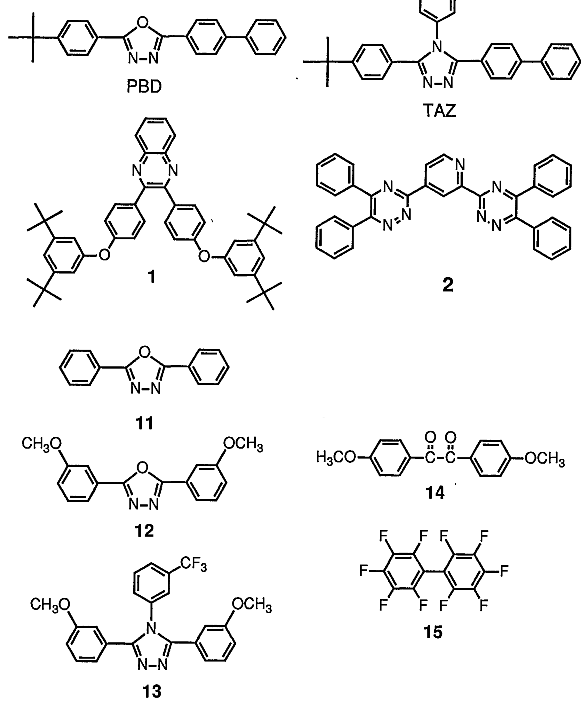

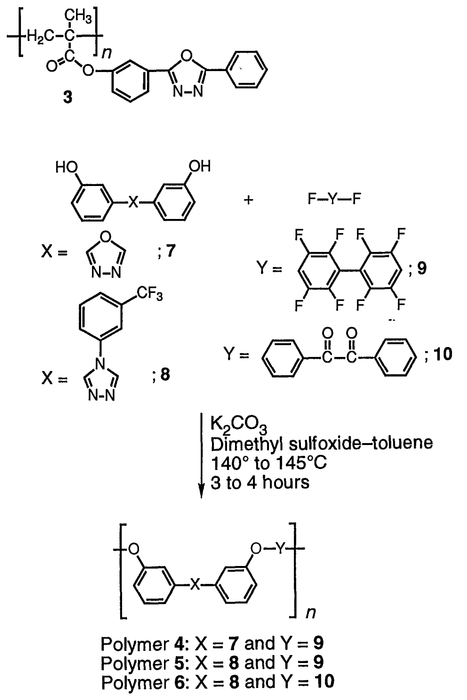

Fig. 3. Polymeric ET materials.

layer (*21*). This result is in contrast to the results of studies of LEDs fabricated without ET layers where the band offset for the majority carrier regulates the current (*8*). The vast improvement in current-carrying capacity afforded by the devices incorporating ET layers leads to crossover into a space charge–limited current regime.

We also found that the most important factor in determining diode stability and yield was the electron transporter used. Devices made with the polymeric electron transporters **4** to **6** exhibited smooth and reproducible current-voltage (*I-V*) characteristics with virtually no change in shape after passing more than 5 to 10 C/cm^2 at currents from 0 to 25 mA/cm^2 (Fig. 4), whereas devices prepared from PBD-PMMA and monomeric **1** and **2** were stable in the current regime from 0 to 10 mA/cm^2 but failed (generally were shorted) after passing <0.5 C/cm^2 at currents of 0 to 25 mA/cm^2. Devices made with polymers **3** to **6** showed no change in performance even after 2 months of storage, and the films themselves remained clear and homogeneous (*22*). The LEDs prepared with films of PBD-PMMA changed most rapidly on storage. The films became cloudy, and the devices were less stable within days of preparation. This response may be attributable to partial crystallization of the PBD and illustrates the importance of designing materials that have high T_g's and covalently attached electroactive components for improving device longevity by suppressing aggregation and phase separation. Thin films of the electron-deficient triazine or quinoxaline heterocyclics (**1** and **2**) were also much less stable than polymers **3** to **6** and exhibited erratic *I-V* characteristics after 2 months of storage. By analogy, we conclude that incorporation of these moieties into amorphous polymers should mitigate this problem (*23*).

In terms of stability during operation for polymeric ET materials, devices prepared with **3** and **5** were the least and most stable, respectively. Diodes prepared with polymer **5** passed as much as 3 ± 0.5 A/cm^2 before failure, whereas those prepared with **3** failed when driven with 0.2 ± 0.03 A/cm^2 (Table 1) (*24*). When PBD-PMMA was the electron transporter, devices failed when 0.1 ± 0.01 A/cm^2 was exceeded. For the polymers, this response may be correlated with the operating voltages, which were the highest for **3** and the lowest for **5**. The substantially higher current-carrying capacity of LEDs containing **5** must be related to the electronic structure and nature of traps incorporated in the polymer, because the T_g's and morphologies (that is, amorphous nature) of **3** to **6** are similar.

We believe that the improvements in both stability and power efficiency demonstrated here show the promise of this approach to the rational molecular design of organic materials for electronics. Because the conductivity in most organic materials is *p*-type, this new class of electron transporters should also be useful with other emitters and in other types of devices (*25*).

Table 1. Summary of the properties of the ET materials and the LEDs containing them.

Electron transporter	T_g† (°C)	Reduction potential‡ (V)	I_{max}, (A/cm^2)	Turn-on voltage (V)	Stability (C/cm^2)
PBD-PMMA	*	−1.94	0.1 ± 0.01	18–23	~1
1	77	−1.61		18	~1
2	109	−1.32 and −1.51		27	~1
3	153	**11**§; −2.08	0.2 ± 0.03	28–31	~1
4	176	**12**§; −2.16 **15**§; −2.09‖	0.2 ± 0.03	22–30	>5
5	186	**13**§; −2.2‖ **15**§; −2.09‖	3.0 ± 0.5	6–10	≫20
6	168	**13**§; −2.2‖ **14**§; −1.27	0.5 ± 0.05	17–19	>10

*Crystallizes at 59°C. †The differential scanning calorimetry heating rate used to determine T_g was 10°C/min. ‡Reduction potentials (versus saturated calomel electrode) were obtained in dimethylformamide containing 0.1 M tetrabutylammonium hexafluorophosphate (TBAPF$_6$). The quantity I_{max} is the current at which device failure occurred. We measured stability by pulsing the current from 0 to 250 μA. The stability value reported is the amount of charge passed through the LED before failure, and the number of photons emitted is 1.2 × 10^{14} times this value. §Model compounds from Fig. 2. ‖Irreversibly reduced.

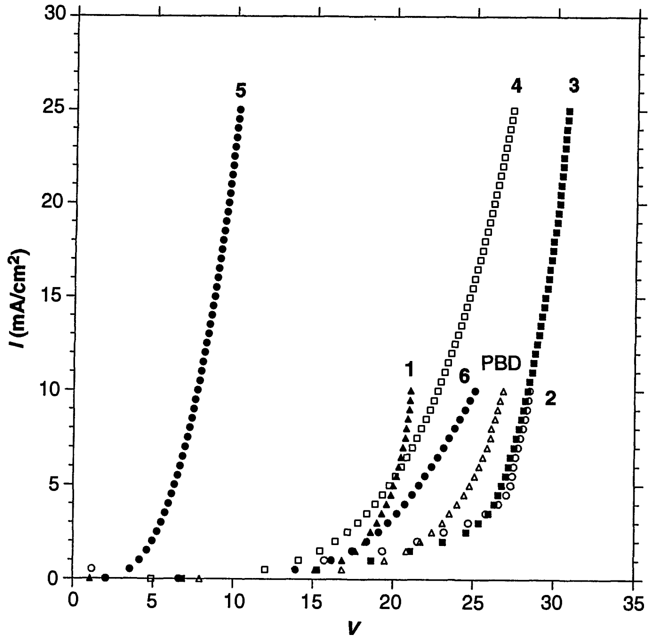

Fig. 4. Current-voltage (*I-V*) characteristics of LEDs as a function of the ET layer.

REFERENCES AND NOTES

1. J. H. Burroughes *et al.*, *Nature* **347**, 539 (1990).
2. D. Braun and A. J. Heeger, *Appl. Phys. Lett.* **58**, 1982 (1991).
3. P. L. Burn *et al.*, *Nature* **356**, 47 (1992).
4. A. R. Brown *et al.*, *Appl. Phys. Lett.* **61**, 2793 (1992).
5. C. Zhang, S. Hoger, K. Pakbaz, F. Wudl, A. J. Heeger, *J. Electron. Mater.* **22**, 413 (1993).
6. N. C. Greenham, S. C. Moratti, D. D. C. Bradley, R. H. Friend, A. B. Holmes, *Nature* **365**, 628 (1993).
7. D. D. C. Bradley, *Synth. Metals* **54**, 401 (1993).
8. I. D. Parker, *J. Appl. Phys.* **75**, 1656 (1994); ———, Q. Pei, M. Marrocco, *Appl. Phys. Lett.* **65**, 1272 (1994).
9. C. Zhang, D. Braun, A. J. Heeger, *J. Appl. Phys.* **73**, 5177 (1993).
10. T. Kanbara and T. Yamamoto, *Chem. Lett.* **1993**, 1459 (1993).
11. C. W. Tang and S. A. Van Slyke, *Appl. Phys. Lett.* **51**, 913 (1987).
12. C. Adachi, T. Tsutsui, S. Saito, *ibid.* **57**, 531 (1990).
13. M. Stolka, J. F. Yanus, D. M. Pai, *J. Phys. Chem.* **88**, 4707 (1984).
14. J. Kido, C. Ohtaki, K. Hongawa, K. Okuyama, K. Nagai, *Jpn. J. Appl. Phys.* **32**, L917 (1993).
15. M. Strukelj, J. C. Hedrick, J. L. Hedrick, R. Tweig, *Macromolecules* **27**, 6277 (1994).
16. The first poly(aryl ether)s containing 2,5-diphenyloxadiaxole in the backbone were prepared from a 4,4′-(isopropylidene)diphenol and 2,5-bis(4-fluorophenyl)-1,3,4-oxadiazole [R. N. Johnson, A. G. Farnham, R. A. Clendinning, W. F. Hale, C. N. Merriam, *J. Polym. Sci. Part A1* **5**, 2375 (1967)]. Recently, the *para*-substituted biphenol and difluoride analogs of **5** and **6** were prepared and incorporated into poly(aryl ether)s [J. W. Connell, P. M. Hergenrother, P. Wolf, *Polymer* **33**, 3507 (1992); J. L. Hedrick and R. Tweig, *Macromolecules* **25**, 2021 (1992)]. Decafluorobiphenyl (*7*) has been incorporated into other types of poly(aryl ether)s [F. Mercer, T. Goodman, J. Wojtowicz, D. Duff, *J. Polym. Sci. Polym. Chem. Ed.* **30**, 1767 (1992); F. W. Mercer, U.S. Patent 5,115,082 (1992)].

17. We prepared the PPV by using a modified version of the Wessling route [R. A. Wessling and R. G. Zimmerman, U.S. Patent 3,401,152 (1968); U.S. Patent 3,706,677 (1972)] as described by F. Papadimitrakopoulos *et al.* [*Chem. Mater.* **6**, 1563 (1994)].
18. We measured the internal quantum efficiencies by placing the LED directly on the Si photodiode and measuring the photocurrent (I_{ph}) as a function of the forward current (I_f). The ratio I_{ph}/I_f was multiplied by 700 to obtain the values.
19. M. Yan, L. J. Rotheberg, F. Papadimitrakopoulos, M. E. Galvin, T. M. Miller, *Phys. Rev. Lett.* **72**, 1104 (1994).
20. Changing substituents on the phenyl groups has only a very small effect on the reduction potentials (for example, compare **11** and **12**).
21. S. M. Sze, *Semiconductor Devices, Physics and Technology* (Wiley, New York, 1985).
22. Devices were stored in an Ar-filled dry box.
23. For example, poly(aryl ether quinoxline)s and poly(aryl ether pyridyltriazine)s. M. Strukelj, J. Hamier, E. Elce, A. S. Hay, *J. Polym. Sci. Polym. Chem. Ed.* **32**, 193 (1994); M. Strukelj and J. C. Hedrick, *Macromolecules* **27**, 7511 (1994).
24. The current was increased from 0 to 50 mA in 200-μA increments over ~90 s.
25. F. Garnier *et al.*, *J. Am. Chem. Soc.* **115**, 8716 (1993); F. Garnier, R. Hajlaoui A. Yassar, P. Srivastava, *Science* **265**, 1684 (1994).

26. The work of M.S. was supported under a Natural Sciences and Engineering Council of Canada postdoctoral fellowship. Useful comments on the manuscript by E. A Chandross, H. Katz, A. Dodabalapur, and M. Galvin are appreciated.

26 October 1994; accepted 25 January 1995

High-Pressure Elasticity of Iron and Anisotropy of Earth's Inner Core

Lars Stixrude*† and R. E. Cohen

A first principles theoretical approach shows that, at the density of the inner core, both hexagonal [hexagonal close-packed (hcp)] and cubic [face-centered-cubic (fcc)] phases of iron are substantially elastically anisotropic. A forward model of the inner core based on the predicted elastic constants and the assumption that the inner core consists of a nearly perfectly aligned aggregate of hcp crystals shows good agreement with seismic travel time anomalies that have been attributed to inner core anisotropy. A cylindrically averaged aggregate of fcc crystals disagrees with the seismic observations.

There is a growing body of seismic evidence that Earth's inner core, a 1200-km solid iron-alloy sphere at the center of our planet, is elastically anisotropic. This observation promises to shed new light on a number of geophysical problems including the crystalline structure of the inner core, its formation by the freezing of the overlying outer core (a process that is thought to be a major energy source driving the fluid motions that produce the geomagnetic field), and the influence of the inner core on the geometry of the geomagnetic field itself.

The seismological data consist of the anomalous splitting of free oscillation frequencies (*1, 2*) and travel time observations (*3–9*), which show that compressional waves that traverse the inner core (*PKIKP*) travel 3 to 4% faster along Earth's spin axis than in the equatorial plane. Most studies agree that the data can be accounted for in terms of cylindrically symmetric elastic anisotropy in the inner core nearly aligned with Earth's spin axis. In detail, inversions of the data are inherently nonunique, and there are important differences among models regarding the magnitude of the anisotropy, its depth dependence, and its degree of alignment with the spin axis. In particular, models based on free oscillation data and those based on travel time observations have been mutually inconsistent. These inconsistencies have led to some doubt about whether the inner core is the source of the anomalous observations (*10*). A recent model (*2*) has been shown to underestimate substantially travel time anomalies along near-antipodal paths (*8, 11*). These inconsistencies, together with our lack of knowledge of the elastic properties of solid iron at inner core pressures (330 to 360 GPa) and temperatures (4000 to 8000 K), have made the seismological observations difficult to interpret in terms of physical models of the origin of inner core anisotropy (*12, 13*).

Here we investigate whether the physical properties of iron are consistent with anisotropy in Earth's inner core. We describe forward models of the inner core based on predictions of the elasticity of iron at high pressure from solid-state theoretical methods. Our approach, which is independent of seismological data, is able to explain a large part of the travel time observations and provides substantial support for the hypothesis of inner core anisotropy.

We assume, in accord with previous work, that the inner core is composed of nearly pure iron (*14, 15*) and that the seismically observed anisotropy is the result of intrinsic crystalline anisotropy. The latter assumption is natural because all known phases of iron either are strongly elastically anisotropic at ambient pressure or are likely to be so on the basis of analog compounds (*16–18*). The stable phase of iron at inner core conditions is unknown. Of the known phases of iron, we consider face-centered-cubic (fcc) and hexagonal close-packed (hcp) but not body-centered-cubic (bcc) as this phase is elastically unstable at high pressure and is thus not expected to exist in the inner core (*19*).

Our calculations are based on a Slater-Koster total energy, tight-binding Hamiltonian (*20, 21*). The parameters of the Hamiltonian are fitted to the most accurate band structures and total energies of fcc, hcp, and bcc phases available from full-potential, linearized augmented plane wave (LAPW) calculations in the generalized gradient approximation performed over a range of volumes that span Earth's pressure regime (*19*). The LAPW calculations are parameter-free and are completely independent of experimental data. With the tight-binding Hamiltonian, we are able to compute properties orders of magnitude faster than with the LAPW method but with no significant loss of accuracy.

We determined the single-crystal, elastic-constant tensor, C_{ijkl}, of each phase at the seismologically observed density of the inner core (*22*) by calculating total energies with the Slater-Koster Hamiltonian as a function of high-symmetry lattice strains (*23*). We fully account for coupling of the elastic constants in hcp to zone-center vibrational modes. The calculated elastic constants (Table 1) completely determine the single-crystal elastic wave velocities for

Table 1. Elastic properties of single-crystal fcc and hcp iron (ρ = 13 Mg/m^3), a cylindrically averaged fcc aggregate [$\langle$fcc$\rangle_{cyl}$ (see text)], and at the surface of a recent, depth-dependent inverse model of the inner core. Normal mode observations constrain three combinations of elastic constants: $\alpha = (C_{33} - C_{11})/A_0$, $\beta = (C_{44} - C_{66})/A_0$, and $\gamma = (C_{12} - C_{13})/A_0$, where $A_0 = \rho V_{P0}^2$; α, β, and ε determine the anisotropy of P, S_{eq}, and S_{me} waves, respectively (*2, 29*).

Parameter	fcc	hcp	$\langle$fcc$\rangle_{cyl}$	Inner core (*2*)
C_{11} (GPa)	1658	1801	1936	
C_{12}	941	865	848	
C_{44}	636	445	451	
C_{33}		1919	2028	
C_{13}		810	1206	
α (%)		+6.5	+4.9	+6.8
β		−1.3	−4.9	−0.9
γ		+3.1	−19.1	−2.3
$\varepsilon = (\alpha - 4\beta + 2\gamma)/4$		+4.5	−3.4	+1.5

L. Stixrude, Institut für Geophysik, Universität Gottingen, 37075 Gottingen, Germany.
R. E. Cohen, Geophysical Laboratory and Center for High Pressure Research, Carnegie Institution of Washington, Washington, DC 20015, USA.

*On leave from the School of Earth and Atmospheric Sciences, Georgia Institute of Technology, Atlanta, GA 30332, USA.

†To whom correspondence should be addressed.